polymers

MDPI

Article

Design of Functional Fluorine-Containing Coatings for 3D-Printed Items

Fedor Doronin *, Georgy Rytikov, Andrey Evdokimov, Mikhail Savel'ev, Yuriy Rudyak and Victor Nazarov

Faculty of Printing Industry, Moscow Polytechnic University, 107023 Moscow, Russia
* Correspondence: f.a.doronin@mospolytech.ru

Abstract

In this study, a surface texture design technique for 3D-extruded prototype products was developed. The study determines some target functional properties of polymer-made items. Four series of experimental samples (acrylonitrile–butadiene–styrene (ABS), thermoplastic polyurethane (TPU), polylactide (PLA), and polyethylene terephthalate glycol (PETG)) were 3D-printed using the fused filament fabrication (FFF) approach. The morphology and hydrophilic/hydrophobic balance of the surfaces of the experimental samples were regulated directly by the 3D design and by gas-phase fluorination techniques. The observed distilled water and ethylene glycol edge wetting angles of the surfaces of the experimental samples were determined by a 3D filament stroke arrangement. It was shown that varying the 3D design promoted hydrophobization and provided anisotropic wetting (the distilled water edge angle of the same sample varies from 76 to 116 degrees). The textured surfaces simultaneously demonstrated hydrophilicity in one direction and hydrophobicity in the other. The changing of the fluorine-containing gas mixture surface treatment duration allowed us to alter the hydrophilic/hydrophobic balance of 3D-extruded prototypes. The fluorination kinetics of the experimental samples were studied empirically. The combination of macroscopic surface design (through FFF 3D printing) and microscopic surface modification (through gas-phase fluorination) permitted a significant reduction in the straining friction coefficient and increased the wettability of the complex-shaped 3D-printed products.

Keywords: surface design; additive manufacturing; FFF; ABS; PLA; TPU; PETG; filament; fluorination; wetting; friction; SEM; morphology

check for updates

Academic Editors: Anton Ficai and Cristina-Elisabeta Pelin

Received: 18 September 2025
Revised: 13 October 2025
Accepted: 14 October 2025
Published: 23 October 2025

Citation: Doronin, F.; Rytikov, G.; Evdokimov, A.; Savel'ev, M.; Rudyak, Y.; Nazarov, V. Design of Functional Fluorine-Containing Coatings for 3D-Printed Items. *Polymers* **2025**, *17*, 2824. https://doi.org/10.3390/polym17212824

Copyright: © 2025 by the authors. Licensee MDPI, Basel, Switzerland. This article is an open access article distributed under the terms and conditions of the Creative Commons Attribution (CC BY) license (https://creativecommons.org/licenses/by/4.0/).

1. Introduction

The creation of polymer-based materials with various special properties (heavy, conductive, and chemo- and/or bio-resistant) is one of the mainstream directions of research and development in the field of modern materials science and applied chemistry [1–3]. The corresponding products are designed to reduce the rate of biogrowth on marine vessels, for medical and pharmacological purposes, to seal friction units in aviation, ship, and mechanical engineering, etc. [1–6].

Considerable attention is paid to various methods of forming functional coatings on the surfaces of metal, ceramic, and polymer materials-based items [7–10]. An experimental assessment of modified polyethylene-based thin-film coatings was carried out in [11,12]. The biological, chemical, and tribological "usefulness" of surface modification was also demonstrated in [13–16].

There are several approaches to the formation of thin-film coatings (from gluing or applying a "ready-made" protective film to polymerization of twisted fluorinated monomers) [17–19]. Each approach is characterized by certain resource and energy intensities, environmental friendliness, ergonomics, and duration of the formation process, thus producing coatings with a range of physicochemical characteristics (wettability, permeability, strength, etc. [20–23]). And there are optimal conditions for the implementation of each modification technique to ensure that the best functional characteristics are achieved in the development of materials [24–26].

It is known that due to the peculiarities of chemical structure and morphology, the fluorinated polymers have low water and air permeability, electrical insulating properties, and high chemical and heat resistance [27–31]. The authors of [32–34] are devoted to the fluorination of polyethylene terephthalate, and the authors of [35,36] investigate polystyrene. The issues of fluorination of polyvinyltrimethylsilane and polyphenylene oxide were investigated in [37,38]. A method of selective modification of polymer films based on a combination of fluorination, sulfonation, and photolithography is presented in [12]. It is devoted to the creation of mosaic thin-film coatings for which the wettability depends on the topographic location of a liquid drop on the wetted surface. The original technologies of gas-phase and plasma-chemical modification are presented in [39–41]. They have been proven to be effective in providing chemical resistance and mechanical strength in a number of polymers with respect to shear tangential deformations [42,43].

A well-known alternative to additive thin-film coating formation is liquid-phase physical modification [44,45]. An example of its implementation is the deposition of nano- or submicron particles from colloidal solutions onto the surface of a substrate [46,47]. Carbon nanotubes (CNTs) are actively used as such particles [48,49]. The issues of CNT synthesis, property analysis, and practical applications are presented in [50–52]. But it seems that, for the field of application under consideration, particle deposition is unacceptable for the functional coating formation due to the low micromechanical strength of the structures being formed and the relatively high cost of such implementation. In addition, the adhesive contact of additive coatings with the substrate is almost always lower than in the case of coatings organically integrated with the volume of the material [53–55].

Thus, the methods for modifying the surface of polymer materials are highly effective and have been sufficiently studied. They allow us to create chemically resistant coatings that are integrated with polymer films and plates. This allows us to expect their successful application in the formation of integrated functional coatings on 3D-printed products.

Some approaches and methods for morphological kinetics modeling of surface modification processes of polymer products and corresponding integrated thin film coatings are presented in [56,57]. Particular fluorination kinetics models for polybuta-diene, polysulfone, and polycarbonate siloxane have been proposed and generalized in [58,59]. The influence of chemical structure and surface microrelief on adhesive and chemical properties of modified polymer layers was considered in [60–62].

The main techniques of the polymer materials chemical structure being studied are the IR-Fourier spectroscopy [63–65]) and scanning electron microscopy (in the mode of mapping the polymer matrix chemical elements' distributions over the surface of the modified polymer layers) [66–68]. The nanorelief structure can be fixed by means of atomic force, scanning electron, and high-resolution optical microscopy [69–71]. An original technique for analyzing the corresponding images of the experimental samples' surface in order to quantify the observed morphological heterogeneity is presented in [72–74].

The purposes of this work are the comprehensive study and the comparative analysis of the macroscopic texture design and the gas-phase fluorination technological parameter effect on the morphology and the energy state of the 3D-printed test products' surface.

2. Materials and Methods

2.1. The Macroscopic Texture Design of 3D-Printed Products' Surface

Twelve series of the experimental samples with 40 mm × 40 mm× 0.8 mm dimensions were produced to study the surface textural design ("linear", "diagonal", and "concentric") effect on the properties of the 3D-printed products made of ABS, PLA, PETG, and TPU filaments using identical FFF 3D printers (Anycubic Kobra Go Shenzhen,, China) (Figure 1).

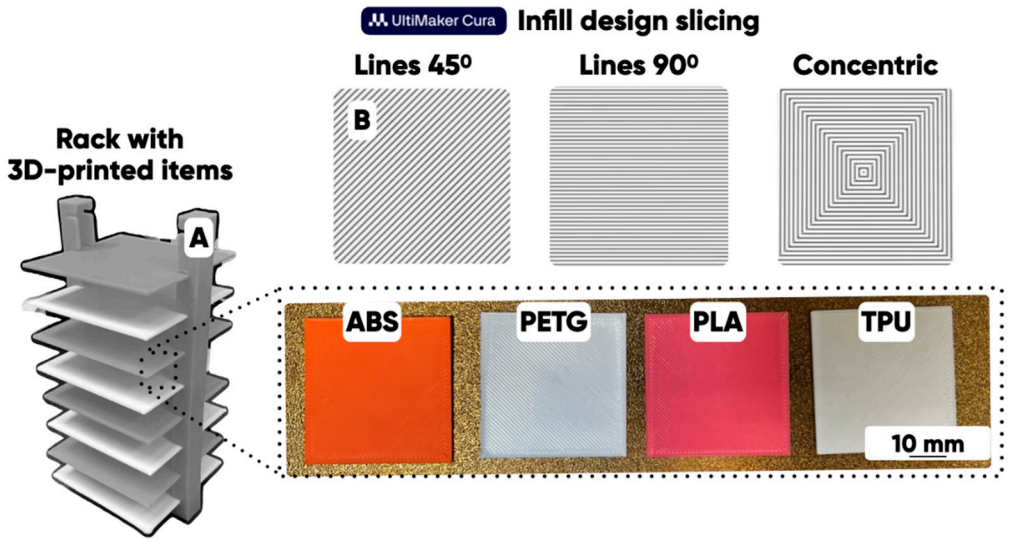


Figure 1. The ABS-, PETG-, PLA-, and TPU-filament-made test products (**A**) prototyped with the identical Anycubic Kobra Go FFF 3D printers and the texture design options, and (**B**) constructed using the UltiMaker Cura computer program (version 5.11-alpha) for 3D rasterization (slicing).

The values of the 3D printing technological parameters (the temperature of the dye, the temperature of the printing platform, and the 3D printing speed) used are shown in Table 1.

Table 1. The 3D printing technological parameters and filament polymer types used when the experimental samples additive prototyping.

Type of Polymer (Filament)	Manufacturer	3D Printing Options		
		Nozzle Temperature, °C	Printing Platform Temperature, °C	Printing Speed, mm/min
Acrylonitrile, butadiene and styrene copolymer (ABS)	Shenzhen Esun Industrial Co., Shenzhen, China	250	80	40
Polylactide (PLA)		210	50	40
Polyethylene Terephthalate Glycol (PETG)		235	60	40
Thermopolastic polyurethane (TPU)	U3print, Moscow, Russia	210	60	30

An increase in the 3D-printed products' quality level (a decrease in the number of observed structural defects) can be achieved as a result of adjusting the Flow parameter at the prepress stage (during the 3D model-based STL file slicing) [43]. It was taken into account in this work during the 3D-printed products manufacturing (Figure 1A).

2.2. The Microscopic Texture Design of the 3D-Printed Products' Surface

Surface properties of the polypropylene-based substrate and the 3D-printed test product's direct control were carried out using the original gas-phase fluorination technique (Figure 2). A fluoro–helium mixture with a fluorine content of 13.5 vol.% (and 86.5 vol.% of helium) was used in accordance with the procedure [75] for the modification. The gas-phase fluorination duration was 0.25, 0.5, and 1.0 h.

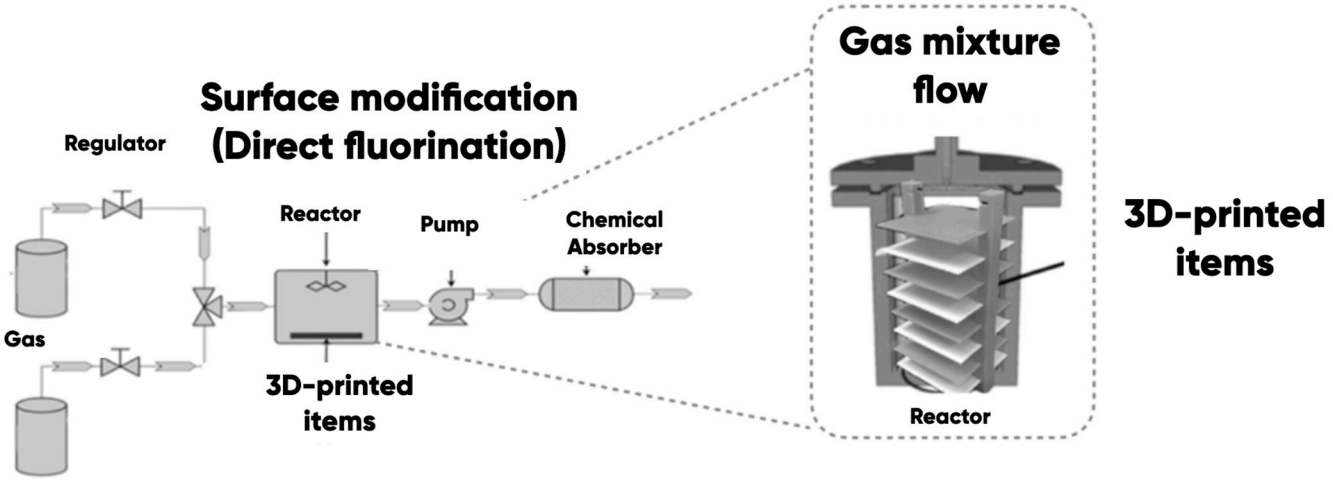


Figure 2. The scheme for 3D-printing product surfaces with the fluorine-containing gas mixture modification technique.

During the preparation stage for modification, the surface of the samples was cleaned from contamination using a mechanical and chemical method (wiping with ethyl alcohol and drying under normal conditions for a day). The experimental samples were then placed into a reaction chamber and degassed by vacuum.

The fluorination of polymer products was carried out in a static mode. The samples were placed in a 5 L steel reactor. The fluoro-helium mixture ($He/F_2 = 86.5/13.5$ vol.%) was introduced into the pre-vacuumed reactor chamber at the atmospheric pressure (10^5 Pa) under the room temperature (20 ± 2 °C).

The gas-phase reaction products were removed by vacuuming and disposed of using standard chemical absorbers after the expiration of the time interval planned by the experimental program. Experimental samples were removed after the reactor chamber was de-vacuumed.

2.3. The 3D-Printed Products' Surface Structure and Properties Studying

The experimental samples' fluorination efficiency was characterized gravimetrically:

- The sample's mass changing due to the gas-phase fluorination was determined using precision scales;
- The degree of fluorination $C_A^F(g/m^2)$ was calculated as a quotient of the induced mass increment by the sample's surface area.

An empirical study of the experimental samples' morphology was carried out using the scanning electron microscopy (SEM) (Jeol JSM 7500 (Tokyo, Japan)) and the infrared frequency range electromagnetic radiation absorption Fourier spectroscopy (IRFS) (Simex FT-801 IR spectrometer (Novosibirsk, Russia)) techniques.

Experimental samples' surface wetting edge angles with the distilled water and the ethylene glycol were measured using the specialized KSVCAM 101 equipment (KSV Instruments, Helsinki, Finland) (Figure 3).

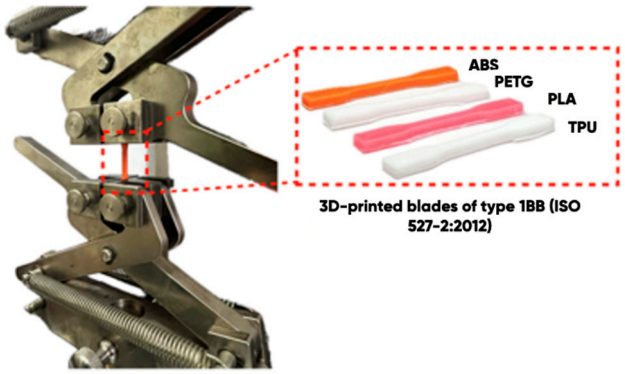


Figure 3. 1BB-type 3D-printed blades.

The specific surface free energy $\gamma_S\left(\mathrm{mJ/m^2}\right)$ calculation (its polar γ_S^P and disperse γ_S^D components) was carried out using the Owens–Wendt–Rabel–Kaelble (OWRK) technique [76–78] taking into account the Girifalco–Good–Fowkes study [79–82].

The effect of gas-phase fluorination on the 1BB-type 3D-printed blades' deformation strength was evaluated using a Zwick Roell BZ1.0 universal bursting testing machine. The straining friction coefficient was measured using a universal friction machine (MTU-01, Saint Petersburg, Russia).

2.4. The Variation–Rotational Maps Creation Technique

The digital SEM-image is formed as a tabular function $L(x,y)$ of pixels' lightness L that depends on the corresponding coordinates (x,y). This image can be cloned with the rotation to some angle φ. It is only necessary to calculate the coordinates as follows:

$$\begin{pmatrix} \widetilde{x}_\varphi \\ \widetilde{y}_\varphi \end{pmatrix} = \begin{pmatrix} cos\varphi & sin\varphi \\ -sin\varphi & cos\varphi \end{pmatrix} \cdot \begin{pmatrix} x \\ y \end{pmatrix} \quad (1)$$

and to implement the assignment operation as follows: $\widetilde{L}(x,y) = L\left(\widetilde{x}_\varphi, \widetilde{y}_\varphi\right)$.

One can obtain the distribution maps of the average values $\overline{L}(x,y)$, standard deviations $\sigma_L(x,y)$, and variation coefficients of $V_L(x,y)$, where

$$\overline{L}(x,y) = \sum_{\varphi=\varphi_1}^{\varphi_N} L_\varphi(x,y)/N \quad (2)$$

$$\sigma_L(x,y) = \sqrt{D_L(x,y)},\ D_L(x,y) = \sum_{\varphi=\varphi_1}^{\varphi_N} \left(L_\varphi(x,y) - \overline{L}(x,y)\right)^2/(N-1) \quad (3)$$

$$V_L(x,y) = \sigma_L(x,y)/\overline{L}(x,y) \quad (4)$$

Averaged values of the variation coefficients should be used as the main quantitative character of the analyzed SEM-image rotational anisotropy.

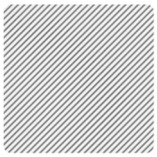
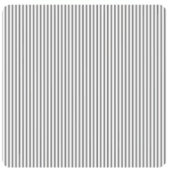
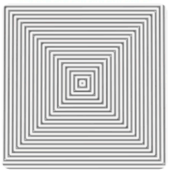
3. Results and Discussion

3.1. The Surface Design Effect on the 3D-Printed Product Wettability

The 3D-printed products' macroscopic surface design significantly affects their actual observed wettability (for PLA—31 $\mathrm{mJ/m^2}$ [83], for TPU—34 $\mathrm{mJ/m^2}$ [84], for ABS—33 $\mathrm{mJ/m^2}$, and for PETG—38 $\mathrm{mJ/m^2}$ [85]). Table 2 shows the results of measuring the surface wetting of the samples (with distilled water and ethylene glycol). Although the experimental samples were made from the same material, the values of specific valid free energy components differ significantly and depend on the direction in which the drop

profile is projected (in a coordinate system determined by the sample surface texture) during measurement.

Table 2. Distilled water and ethylene glycol wetting edge angles and the corresponding values of the specific free surface energy (total, dispersion, and polar components) for the PLA-based 3D-printed samples at different macroscopic surface design (filament strokes orientation).

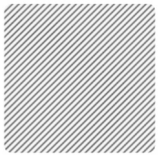
3D-Printed Product Surface Macroscopic Textural Design	Wetting Edge Angle, ° θ_{H_2O}	$\theta_{C_2H_6O_2}$	γ,mJ/m^2	γ_S^D,mJ/m^2	γ_S^P,mJ/m^2
Lines 45⁰ 	74 ± 7	46 ± 6	35 ± 4	24 ± 2	11 ± 2
Lines 90⁰ 	76 ± 8	59 ± 6	31 ± 3	12 ± 1	16 ± 2
Lines 90⁰ 	116 ± 8	91 ± 8	19 ± 3	18 ± 3	1 ± 1
Concentric 	106 ± 8	65 ± 7	52 ± 5	51 ± 1	1 ± 1

It should be noted that Table 2 shows the results of wetting angle measurements along the same direction in the laboratory coordinate system. Droplets on the surfaces under consideration are elongated along the 3D strokes and, as a result, the wetting angle depends on the direction of measurement. Macroscopic texturing provides actual wetting anisotropy due to differences between the surface of 3D-printed products and the plane. This anisotropy will not be visible to the naked eye in materials made of films.

But even the minimum observed wetting angle is large enough for the application of functional layers to the surface of test products, so an adhesive must be added to the ink composition.

The previously proven gas-phase fluorination technique [86] was applied to increase the wettability of the 3D-printed products surface. Corresponding results are presented in Table 3.

Table 3. The distilled water and ethylene glycol wetting edge angles and the corresponding values of the specific free surface energy (total, dispersion, and polar components) for the TPU-, ABS-, PLA-, and PETG-made 3D-printed samples after the fluorination at different durations.

3D-Printed Product Surface Macroscopic Textural Design	Filament Type	Wetting Edge Angle, ° θ_{H_2O}	$\theta_{C_2H_6O_2}$	γ,mJ/m^2	γ_S^D,mJ/m^2	γ_S^P,mJ/m^2
		Fluorination Duration (0 h)				
Lines 45º 	TPU	85 ± 9	48 ± 5	42 ± 4	40 ± 4	2.0 ± 0.5
	ABS	67 ± 7	62 ± 6	37 ± 4	3.2 ± 0.5	35 ± 4
	PETG	79 ± 8	51 ± 5	41 ± 4	8.0 ± 0.8	33 ± 4
	PLA	74 ± 7	46 ± 5	35 ± 4	24 ± 2	11 ± 2
		Fluorination duration (0.25 h)				
	TPU	49 ± 5	22 ± 2	50 ± 5	15 ± 2	36 ± 4
	ABS	59 ± 6	19 ± 2	46 ± 5	27 ± 3	19 ± 2
	PETG	68 ± 7	28 ± 2	44 ± 4	34 ± 3	10 ± 2
	PLA	56 ± 6	26 ± 2	45 ± 4	19 ± 2	26 ± 3
		Fluorination duration (0.5 h)				
	TPU	59 ± 6	24 ± 2	44 ± 5	24 ± 3	20 ± 2
	ABS	51 ± 5	14 ± 2	49 ± 5	20 ± 2	29 ± 3
	PETG	58 ± 6	22 ± 2	45 ± 5	24 ± 3	21 ± 2
	PLA	63 ± 6	34 ± 3	41 ± 4	21 ± 2	19 ± 2
		Fluorination duration (1 h)				
	TPU	48 ± 5	20 ± 2	51 ± 5	15 ± 2	36 ± 4
	ABS	45 ± 5	18 ± 2	53 ± 5	13 ± 2	40 ± 4
	PETG	52 ± 5	23 ± 2	33 ± 4	25 ± 3	7.7 ± 0.8
	PLA	43 ± 4	17 ± 2	55 ± 6	12 ± 1	43 ± 4

It can be seen (Figure 4) that in all cases, the surface wettability of experimental samples increases significantly. However, this is accompanied by multidirectional changes in the components of the specific free surface energy and various types of induced transformations of the experimental sample surface energy state. The largest increase in the specific free surface energy was observed for PLA (from 35 to 55 mJ/m^2). It is explained by a more than fourfold increase in surface energy polar component (γ_S^P)—from 11 to 43 mJ/m^2. The change in the wettability of TPU is also mainly due to an increase in the polar component of the specific free surface energy, whereas for ABS and PETG, there is a significant increase in the one for dispersion (compared with the initial values).

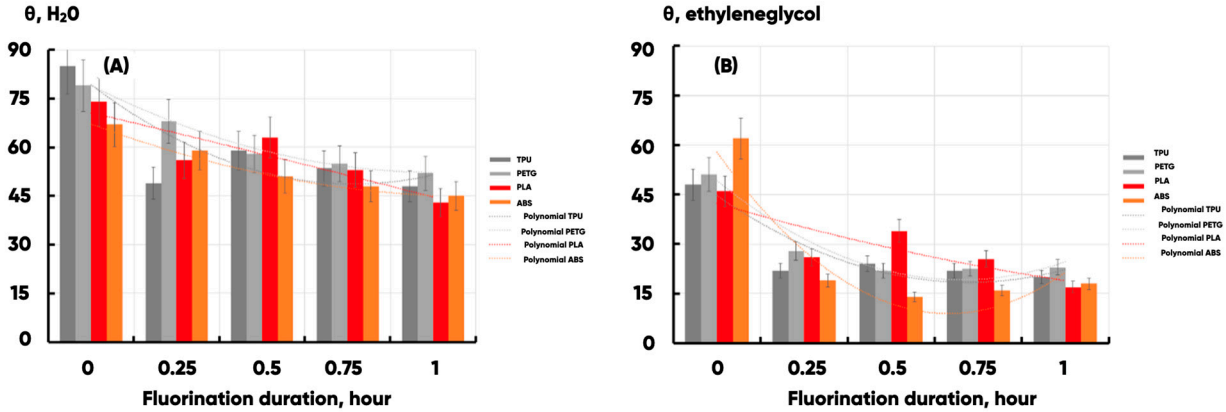


Figure 4. The water (**A**) and the ethylene glycol (**B**) wetting edge angle (θ_{H_2O} and $\theta_{C_2H_6O_2}$) dependencies on the fluorination procedure duration (T, hour) for the PETG-(light gray), TPU-(light dark gray), PLA-(red), and ABS-(orange) based samples. Second-order polynomials were used for the approximation in all cases.

It is known that the surface wettability is significantly affected by its chemical and physical structure (this follows from the possibility of appropriate Gibbs energy factorization). Changes in the chemical composition and surface structure of the filament during its curing are due to various factors, including the elemental composition, chemical structure, temperature and speed of extrusion, air (atmospheric) composition, and other conditions under which curing takes place. In particular, short-term exposure to elevated temperatures can lead to some oxidation of the surface, which contributes to hydrophilization.

3.2. The Effect of the Fluorination on 3D-Printed Product Surface Morphology

Obtained values of the modification degree C_A^F, g/m^2 (calculated as the ratio of the sample mass change to its surface area) are significantly higher for the 3D-printed materials (Table 4) than for the large-tonnage polyolefins- (polyethylene, polypropylene, polyvinyl chloride, and polyethylene terephthalate) made films and for the elastomers- (butyl rubber, nitrile butadiene rubber, ethylene propylene triple rubber copolymer, etc.) based plates [61,87].

Table 4. The ABS-, PLA-, TPU- and PETG-made 3D-printed test products' fluorination degree for different durations of gas-phase processing.

Modification Duration, h	3D-Printed Products' Fluorination Degree C_A^F,g/m^2			
	ABS	PLA	TPU	PETG
0.25	4.1 ± 0.4	2.8 ± 0.2	2.3 ± 0.2	5.3 ± 0.4
0.5	17.5 ± 0.8	7.0 ± 0.5	8.0 ± 0.5	7.3 ± 0.5
1.0	21.9 ± 0.8	13.3 ± 0.5	22.2 ± 0.8	13.0 ± 0.5

The significant differences in the 3D-printed samples' fluorination degree from ones for polymer material-made films and plates are due to the following:

(a) The presence of pores (with the diameters of 50 nm or more) in the initial and in the modified experimental samples structure contributing to the effective diffusion of the active reagent (fluorine) and significantly increasing the interaction with the modified gas mixture 3D-printed product surface area (Figure 5).

(b) The presence of unsaturated bonds in the 3D-printed polymers' macromolecules (Table 5), which contribute to the intensive course of fluorine addition reactions.

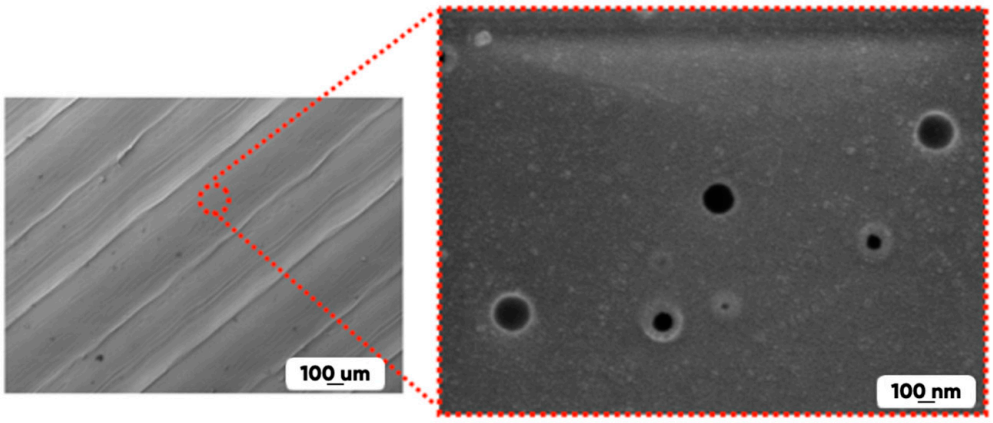
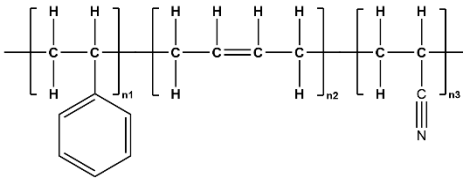
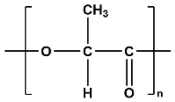
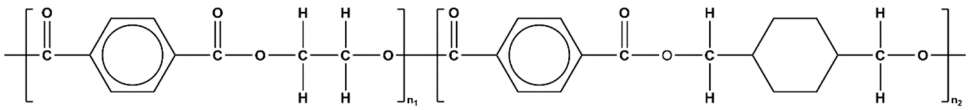
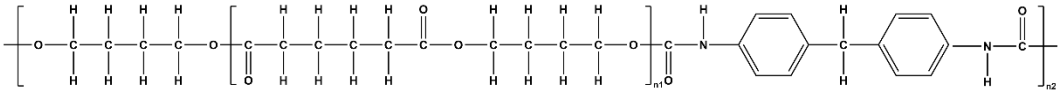


Figure 5. The multi-scale SEM-images of the PLA-made 3D-printed products' surface.

Table 5. The chemical structure of 3D-printed materials under consideration.

Abbreviation	Chemical Formula
ABS [88]	
PLA [89]	
PETG [90]	
TPU [91]	

The effect of the fluorination on the macroscopic structure of the 3D-printed products' surface manifested itself in the form of distortion and/or disappearance of the boundaries between the adjacent 3D-strokes (Figure 6). It is probably caused by the thermally induced melting of the bulges with the largest specific area of active reagent contact (the fluorination and oxidation reactions are exothermic).

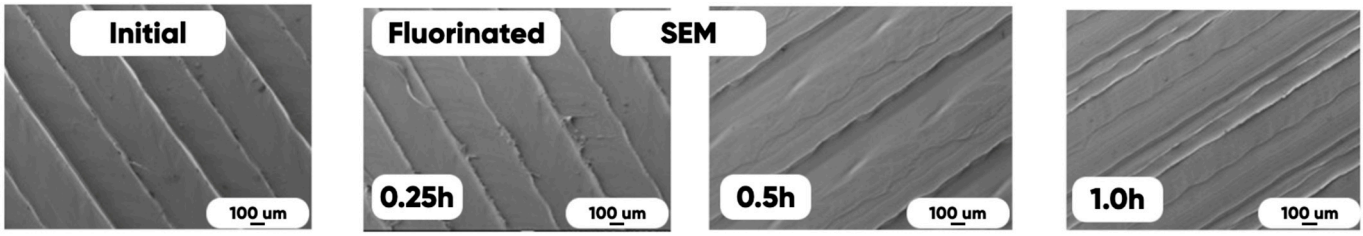


Figure 6. The SEM-images of the initial and the 0.25, 0.5, and 1.0 h fluorinated thermoplastic polyurethane samples.

The parameters (for example, "period" and "borehole") described the well-observed periodic elements of the 3D-prototypes' macroscopic surface texture depending on the geometric design of the surface, the slicing settings, the diameter of the 3D-printer die, the extrusion speed of the filament, and the speed of 3D-printer's printhead movement. The surface structure is formed as a result of the 3D-strokes coming into contact with each other.

The macroscopic texture of non-periodic elements, which are poorly observed with the naked eye at a macroscopic scale, depends more on the temperature of the filament, its melt fluidity index, and the curing rate, since they are the result of self-organization of the material structure after phase transition. They can also affect wettability due to changes in the true surface area. Thus, 3D-printed product macroscopic surface textures are mainly determined by relative position and 3D-stroke dimensions.

Thus, 3D-products' actual surface areas are significantly larger than the areas of their projections onto the plane of the 3D printer's object platform. And the degree of their difference from each other is determined by the sizes and the features of the relative arrangement of the fully macroscopic 3D-strokes that forming the 3D-prototypes following the "surface design".

At the microscopic level, the gas-phase modification by a fluorine-containing gas mixture had a significant effect on the nature of the planar distribution of the material-forming elements. Figure 7 shows the distribution maps of carbon, oxygen, nitrogen, and fluorine obtained by X-ray photoelectron spectrometry technique for the initial and the modified samples of thermoplastic polyurethane within 0.25, 0.5, and 1.0 h of gas-phase treatment. The carbon planar distribution actually repeats the surface microrelief.

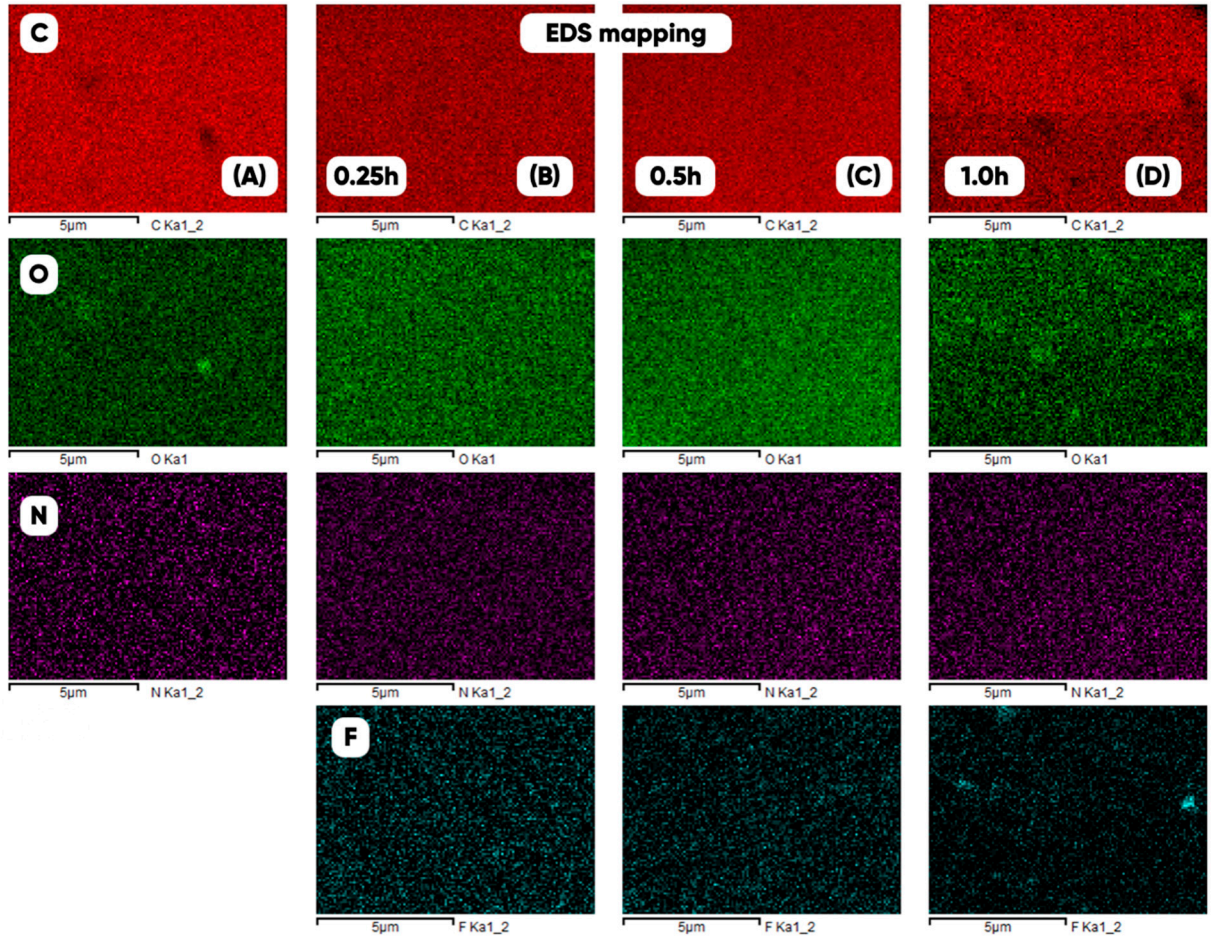


Figure 7. The planar distributions (EDS-mapping) of the carbon (C), oxygen (O), nitrogen (N), and fluorine (F) for the initial (**A**) and the fluorinated (0.25 (**B**), 0.5 (**C**), and 1.0 (**D**) h) 3D-printed products based on thermoplastic polyurethane.

A previously developed approach of variation–rotation patterns [39,42] was applied to quantify the modification influence on the chemo-morphological transformations of the experimental samples' surface structure at the microscopic scale (Table 6). The essence of the method consists of cloning the source images with rotation by a certain angle (in our case by 15 degrees) and calculating main statistical characteristics (average value, standard deviation, and variation coefficient of lightness) for each pixel location in the resulting pattern.

The average value, standard deviation, asymmetry, and kurtosis of the pixel lightness variation coefficients, as well as the size of the chemo-morphological structure stability domain at levels 0.05 and 0.5, are presented in Table 7.

Table 6. Frontal and profile projections of the variation–rotational maps constructed for the planar distributions (Figure 7) of carbon, oxygen, nitrogen, and fluorine. The square side length is ~5 microns.

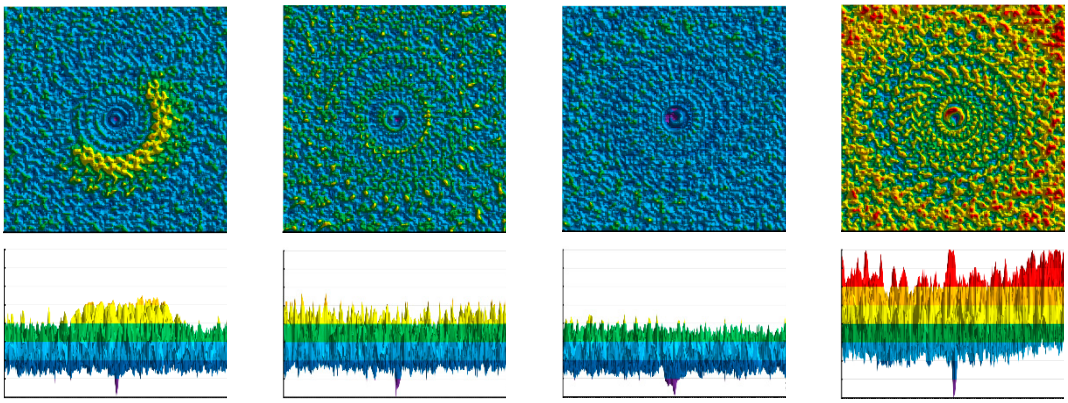
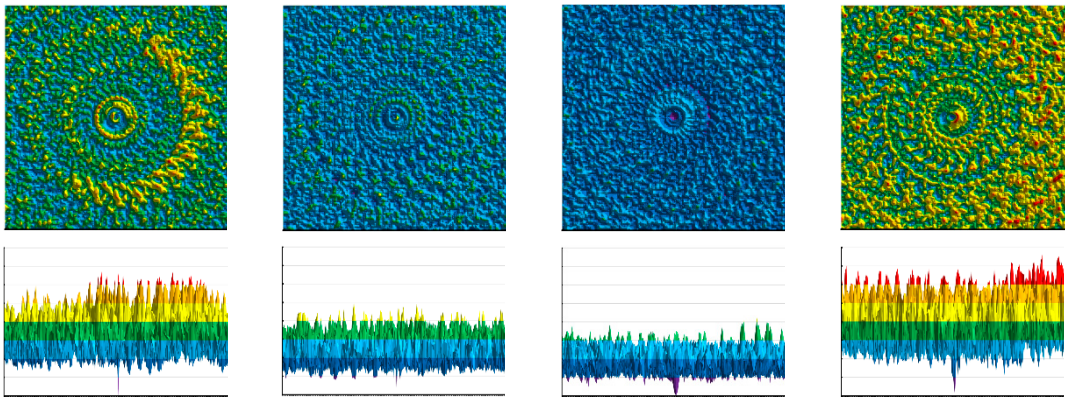
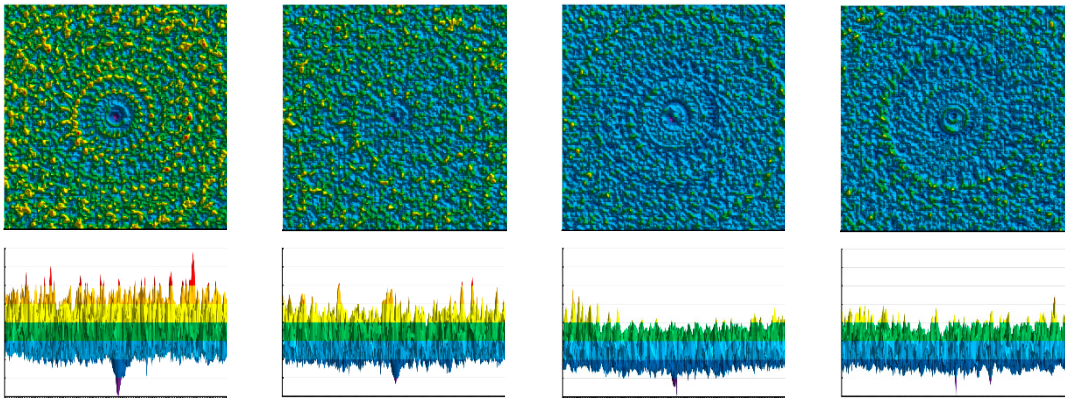
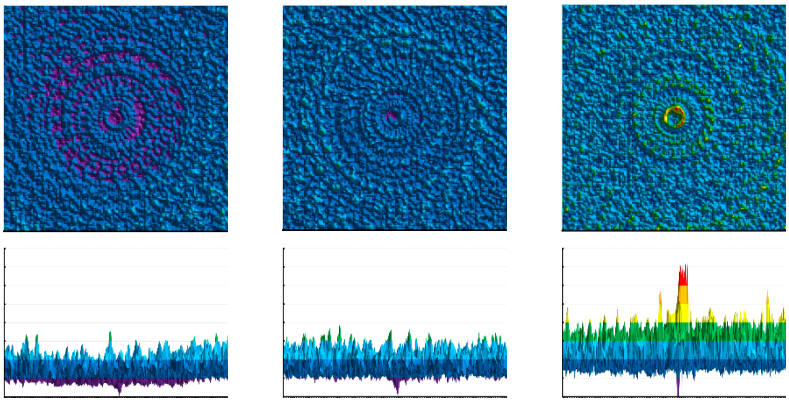
	Fluorination Duration, Hour			
	Initial	**0.25**	**0.5**	**1.0**
C				
O				
N				
F	-			

Table 7. Quantitative characteristics of the variation–rotation patterns formed as a result of the material-forming element (carbon, oxygen, nitrogen, and fluorine) planar distribution (Figure 6) computer analysis.

Gas-Phase Fluorination Duration, Hour	0.00	0.25	0.5	1.0
Carbon Planar Distribution Quantitative Characteristics				
Average value of the variation coefficient	0.13	0.14	0.12	0.21
Standard deviation of the variation coefficient	0.04	0.03	0.03	0.05
Asymmetry of the variation coefficient distribution	0.77	0.37	0.28	0.36
Kurtosis of the variation coefficient distribution	0.87	0.34	0.25	0.07
Structural domain characteristic size (at 0.05 level), nm	120	130	290	60
Structural domain characteristic size (at 0.5 level), nm	5000	5000	5000	5000
Oxygen planar distribution quantitative characteristics				
Average value of the variation coefficient	0.40	0.29	0.23	0.47
Standard deviation of the variation coefficient	0.09	0.07	0.05	0.11
Asymmetry of the variation coefficient distribution	0.53	0.34	0.32	0.29
Kurtosis of the variation coefficient distribution	0.46	0.14	0.29	0.05
Structural domain characteristic size (at 0.05 level), nm	40	40	100	40
Structural domain characteristic size (at 0.5 level), nm	4640	4980	4990	3930
Nitrogen planar distribution quantitative characteristics				
Average value of the variation coefficient	0.89	0.78	0.66	0.66
Standard deviation of the variation coefficient	0.19	0.16	0.14	0.14
Asymmetry of the variation coefficient distribution	0.49	0.50	0.38	0.39
Kurtosis of the variation coefficient distribution	0.78	0.67	0.64	0.34
Structural domain characteristic size (at 0.05 level), nm	50	40	40	40
Structural domain characteristic size (at 0.5 level), nm	510	830	1710	1760
Fluorine planar distribution quantitative characteristics				
Average value of the variation coefficient	-	0.70	0.87	1.16
Standard deviation of the variation coefficient	-	0.20	0.19	0.29
Asymmetry of the variation coefficient distribution	-	0.78	0.57	1.13
Kurtosis of the variation coefficient distribution	-	1.06	0.90	3.43
Structural domain characteristic size (at 0.05 level), nm	-	40	40	60
Structural domain characteristic size (at 0.5 level), nm	-	1940	550	120

All obtained empirical statistical distributions are characterized by a sharper peak than normal ones and are described by an asymmetry in which the mode does not exceed the mathematical expectation. The planar carbon distribution (which largely determines the microtexture of the polymer matrix) is expected to have the highest structural stability (with the minimum average value and standard deviation of the pixel lightness coefficient of the variational–rotational pattern). The lowest structural stability (prior to the modification) is characteristic of the planar nitrogen distribution (the maximum mean and deviation of the coefficient of variation is $V_N \cong 0.9 \pm 0.2$). The fluorine planar distribution becomes least uniform ($V_F \cong 1.2 \pm 0.3$) and the variability of the nitrogen distribution decreases ($V_N \cong 0.7 \pm 0.1$) after the long (1 h) tested sample modification. At the same time, the structural stability of the polymer matrix decreases ($V_C \cong 0.21 \pm 0.05$) and the morphological

heterogeneity of the oxygen distribution during the gas-phase treatment passes through a minimum value ($V_O \cong 0.23 \pm 0.05$). Therefore, it is thus shown that gas-phase fluorination contributes to significant changes in the mode structure of roughness and material-forming elements on the surface of 3D-printed products at the microscopic level.

Results of the elemental analysis of changes in the atomic content of carbon, oxygen, nitrogen, and fluorine due to the gas-phase modification of TPU indicate the nonlinearity of the surface fluorination kinetics of the corresponding 3D-printed test products (Table 8).

Table 8. Results of the elemental analysis of the carbon, oxygen, nitrogen, and fluorine content (excluding hydrogen) in the surface layer of a cured gas-phase-modified thermoplastic polyurethane filament.

Fluorination Duration, Hour	C (at. %)	O (at. %)	N (at. %)	F (at. %)
0	67.0 ± 0.8	25.0 ± 0.8	8.0 ± 0.1	-
0.25	66.0 ± 0.7	24.0 ± 0.7	8.0 ± 0.1	2 ± 0.1
0.5	66.0 ± 0.7	23.0 ± 0.6	7.0 ± 0.1	4 ± 0.2
1	66.0 ± 0.5	18.0 ± 0.4	10.0 ± 0.2	6 ± 0.4

The carbon content in the surface layer of the experimental samples (correlated with the macroscopic features of the microrelief) slightly decreases (at the level of statistical error) due to gas-phase processing. This corresponds to macroscopically observed "blur-ring" of the neighboring 3D-stroke boundaries.

A detailed analysis of the dynamics of fluorination for a number of polymer materials using various approaches to simulation is presented in a large number of scientific papers, including some papers written by our research team previously. For example, ref. [56] showed that the distribution of fluorine in modified surface layers was significantly heterogeneous across the surface area, and nonlinear with respect to the depth of penetration of the modifier into the polymer matrix. (Figure 8).

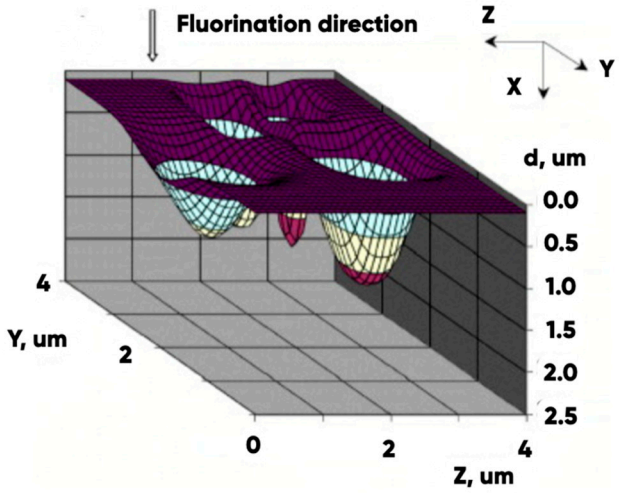


Figure 8. The typical result of polymer material fluorination dynamics simulation [56].

Empirically obtained results of gravimetric measurements (Table 4) and EDS-analysis (Table 8) confirm the typical characteristic of the fluorination process, which is nonlinearity for the considered 3D-printed materials.

A decrease in the atomic oxygen content combined with an increase in the nitrogen content in the analyzed layer, most likely, indicates the destruction of NC bonds in TPU macromolecules accompanied by the addition of fluorine to nitrogen and carbon atoms.

The nonlinearity of the fluorine content change is most likely due to the depletion of the number of CH- bonds in which the hydrogen atoms would not be replaced by the fluorine ones after a long (1 h) gas-phase modification.

The significance of the fluorinated 3D-printed products' surface chemical structure changes is also evidenced by the IR-Fourier spectroscopy results obtained for the ABS-, TPU-, and PP-made samples (Figure 9).

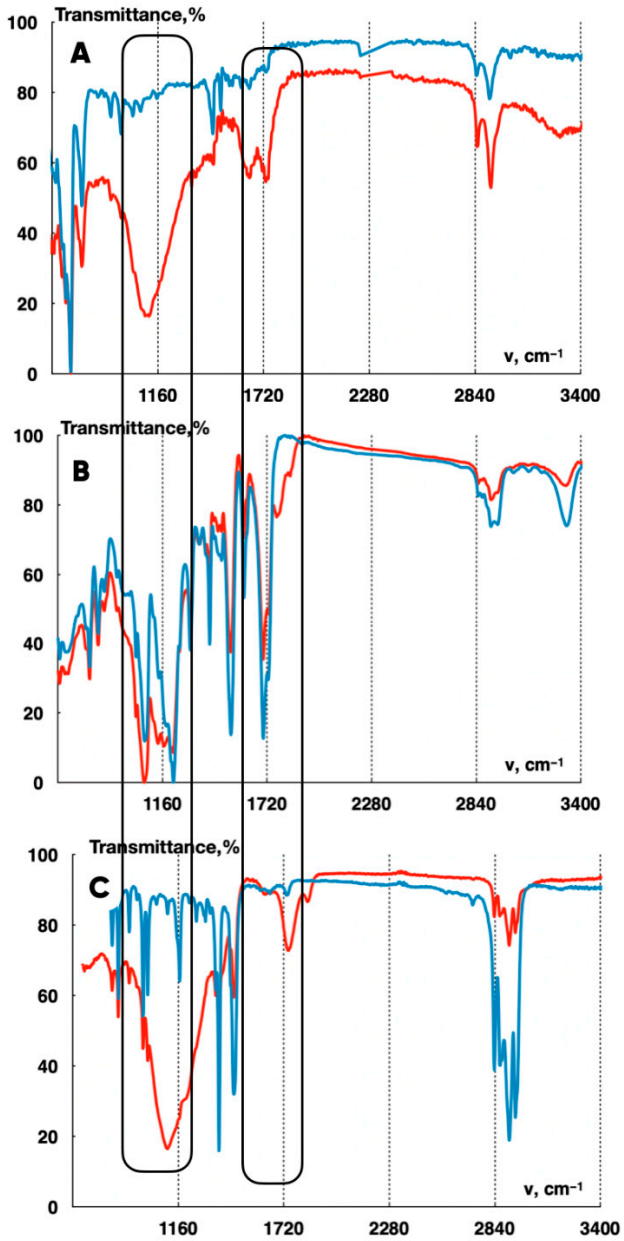


Figure 9. IR-Fourier spectra for the initial and the fluorinated 3D-printed products based on ABS (**A**), TPU (**B**), and polypropylene (**C**) (comparison sample). The blue color indicates the absorption spectra of the infrared electromagnetic radiation for the initial samples; the red indicates the fluorinated ones.

The IR spectra (Figure 9) show that all the considered types of polymers (ABS, TPU, and PP) are characterized by the appearance of a dip with the wave numbers 1100–1365 cm^{-1} corresponding to the valence vibrations of the CF-bonds. The difference in the intensity of the corresponding spectral lines is due to the peculiarities of the polymers' chemical nature.

Chemical transformations of the polymer materials under consideration caused by their induced oxidation (Figure 9A,C) or by the changes in the character of CO-bonds (Figure 9B are accompanied with the increase (Figure 9A,C) or decrease (Figure 9B) in IR-radiation absorption in the 1600–1800 cm^{-1} wave numbers range.

The overall increase in the absorption (10–15%) of the infrared frequency range electromagnetic radiation in the ABS-based samples (Figure 9A) as a result of the fluorination indicates significant changes in the texture and the chemical structure of the corresponding products' surface. The increase in the 2800–2900 cm^{-1} CH-bonds region (Figure 9A) is probably due to the chemo-induced destruction of double C=C bonds and the cycles opening. The decrease in the CH-bonds region (Figure 9B,C) is usually interpreted as a consequence of hydrogen substitution reactions with the fluorine.

The increase in the transmission (in 3000–3400 cm^{-1} range) (Figure 9B) indicates the destruction (as a result of fluorination) of OH-groups formed when the TPU filament comes into contact with the atmospheric moisture during the curing.

It is well-known that polymer product fluorination under extreme conditions can lead to their destruction due to insufficient mechanical strength. It was found (Table 9) that the gas-phase fluorination under the experimental conditions does not affect the tensile strength of 3D-printed blades made of ABS, PLA, TPU, and PETG filaments (the values remain unchanged within the statistical error (Figure 10A).

Table 9. The hardness H (MPa) and the straining friction coefficient μ for the 3D-printed type 1BB tubes before and after the gas-phase fluorination.

Fluorination Duration, Hour	3D-Printing Material							
	ABS		PLA		TPU		PETG	
	H, MPa	μ	H, MPa	μ	H, MPa	μ	H, MPa	μ
0	41 ± 3	1.20 ± 0.10	64 ± 6	0.50 ± 0.05	36 ± 3	0.85 ± 0.08	52 ± 5	1.10 ± 0.10
0.25	44 ± 4	0.92 ± 0.09	68 ± 7	0.41 ± 0.05	39 ± 4	0.70 ± 0.07	52 ± 4	0.88 ± 0.09
0.5	41 ± 3	0.68 ± 0.07	67 ± 7	0.33 ± 0.04	40 ± 4	0.59 ± 0.06	52 ± 3	0.72 ± 0.08
1	43 ± 3	0.22 ± 0.02	65 ± 6	0.21 ± 0.02	41 ± 4	0.41 ± 0.04	52 ± 4	0.43 ± 0.04

At the same time, the strain-induced friction coefficient (maximum rest friction coefficient) significantly decreases, which correlates with an increase in abrasion resistance (Figure 10B). Microscopic transformations of the supramolecular structure of polymer materials caused by changes in the nature of material-forming element (carbon, oxygen, and to some extent nitrogen) planar distributions lead to improvements in the tribological properties of surfaces.

Thus, the demonstrated structural, morphological, and chemical transformations of the near-surface and surface layers of 3D-printed products as a result of macroscopic (3D printing) and microscopic (gas-phase modification) design provides the possibility of direct regulation of lyophilic, tribological, and other properties (depending on surface energy state).

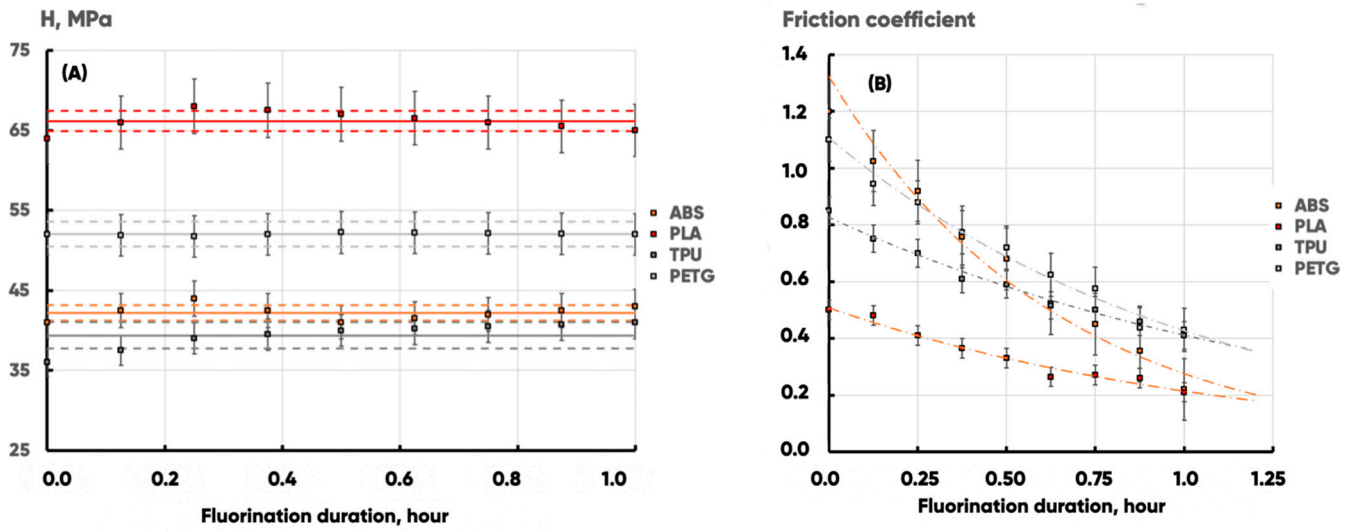


Figure 10. The experimental samples' hardness (H, MPa) (**A**) and straining friction coefficient (μ, un.) (**B**) Dependences on the fluorination procedure duration (T, hour) for ABS (orange), PLA (red), PETG (dark gray), and TPU (light gray). The continuous and dashed lines indicate mean values and confidence intervals in (**A**). The dashed–dotted lines in B are the result of the experimental data exponential approximation.

4. Conclusions

The direct physico-chemical and textural design of the surface was carried out. Texture modeling was performed, and the properties of integrated submicroscopic coatings (obtained as a result of 3D printing of test products' surfaces) were determined. The straining friction coefficient and wettability were experimentally determined.

The straining friction coefficient and wettability were experimentally determined. Interrelationships between microtexture, chemical composition, and structure and functional properties of additive-prototyping polymers were established. Absence of a statistically significant effect of fluorination on deformation strength of 3D-printed test products was demonstrated.

It is shown that the surface design of 3D-printed products promotes hydrophobization and anisotropy of wetting. The distilled water edge angle varies from 76 to 116 degrees for the same sample, simultaneously demonstrating hydrophilicity in one direction and hydrophobicity in the other.

It is established that the gas-phase surface modification technological regime (the duration of the material surface treatment with a fluorine-containing gas mixture) provides the possibility of FFF 3D prototyping products' surface structure direct control at the micro-scale level.

Thus, the combination of the extrusion additive prototyping and the gas-phase surface modification techniques is the most promising way to form the functional (including bio- and chemo-resistant) surface coatings integrated with a polymer matrix volume.

The combination of developed analysis and modeling techniques will allow us to further formulate theoretical descriptions of high-innovation potential technologies for directly controlling the functional properties of bulk modified polymers used in 3D printing.

Such materials can be used in construction, when creating water-resistant materials and sealing products; in medicine, when creating biocompatible products, including biodegradable and bio-resistant ones; and in the automobile industry, such as in panel, chassis elements, suspension, intake manifold, valve cover, and turbocharger housing manufacturing.

Typical limitations of polymer composite use in industry include an insufficiently high level of mechanical strength, low temperature resistance, flammability and toxicity of combustion products, and the complexity of product molding. The advantage of gas-phase fluorination exploitation is the possibility of carrying out the functionalizing finishing surface treatment of 3D-printed items manufactured using already developed and well-proven additive prototyping techniques.

Author Contributions: Conceptualization, G.R. and F.D.; methodology, F.D. and G.R.; software, Y.R.; validation, A.E.; formal analysis, M.S.; investigation, G.R.; resources, V.N. and M.S.; data curation, A.E., writing—original draft preparation, F.D. and G.R.; writing—review and editing, G.R., Y.R. and V.N.; visualization, A.E.; supervision, V.N.; project administration, F.D.; funding acquisition, F.D. All authors have read and agreed to the published version of the manuscript.

Funding: This work was carried out with the financial support of the Ministry of science and higher education of the Russian Federation (State assignment FZRR-2023-0003).

Institutional Review Board Statement: Not applicable.

Data Availability Statement: The original contributions presented in this study are included in the article. Further inquiries can be directed to the corresponding authors.

Conflicts of Interest: The authors declare no conflicts of interest.

References

1. Melnikov, P.; Bobrov, A.; Marfin, Y. On the use of polymer-based composites for the creation of optical sensors: A review. *Polymers* **2022**, *14*, 4448. [CrossRef] [PubMed]
2. Wang, X.; Gou, J.; Jiang, M.; Zhou, Z.; Hui, D. 3D printing of polymer matrix composites: A review and prospective. *Compos. Part B Eng.* **2017**, *110*, 442–458. [CrossRef]
3. Bauhofer, W.; Kovacs, J.Z. A review and analysis of electrical percolation in carbon nanotube polymer composites. *Compos. Sci. Technol.* **2009**, *69*, 1486–1498. [CrossRef]
4. Mayandi, K.; Rajini, N.; Ayrilmis, N.; Indira Devi, M.P.; Siengchin, S.; Mohammad, F.; Al-Lohedan, H.A. An overview of endurance and ageing performance under various environmental conditions of hybrid polymer composites. *J. Mater. Res. Technol.* **2020**, *9*, 15962–15988. [CrossRef]
5. Gao, J.; Wang, L.; Guo, Z.; Li, B.; Wang, H.; Luo, J.; Huang, X.; Xue, H. Flexible, superhydrophobic, and electrically conductive polymer nanofiber composite for multifunctional sensing applications. *Chem. Eng. J.* **2020**, *381*, 122778. [CrossRef]
6. Shojaei, A.; Abbasi, F. Cure kinetics of a polymer-based composite friction material. *J. Appl. Polym. Sci.* **2006**, *100*, 9–17. [CrossRef]
7. Montemor, M.F. Functional and smart coatings for corrosion protection: A review of recent advances. *Surf. Coat. Technol.* **2014**, *258*, 17–37. [CrossRef]
8. Zhang, L.; Zhou, A.G.; Sun, B.R.; Chen, K.S.; Yu, H. Functional and versatile superhydrophobic coatings via stoichiometric silanization. *Nat. Commun.* **2021**, *12*, 982. [CrossRef] [PubMed]
9. Calderon Velasco, S.; Carvalho, S.; Cavaleiro, A. Functional properties of ceramic-Ag nanocomposite coatings produced by magnetron sputtering. *Prog. Mater. Sci.* **2016**, *84*, 158–191. [CrossRef]
10. Verbič, A.; Gorjanc, M.; Simončič, B. Zinc oxide for functional textile coatings: Recent advances. *Coatings* **2019**, *9*, 550. [CrossRef]
11. Nazarov, V.G. Composition and dimensions of the surface and transition layers in modified polymers. *Polym. Sci. Ser. B* **1997**, *39*, 142–145.
12. Nazarov, V.G. Multiple surface structures in polyolefins formed by modification methods. *J. Appl. Polym. Sci.* **2005**, *95*, 1198–1208. [CrossRef]
13. Mahakur, V.K.; Paul, R.; Bhowmik, S.; Patowari, P.K. Influence of surface modification on mechanical and tribology performance of jute filler polymer composites and prediction of the performance using artificial neural network. *Polym. Bull.* **2023**, *80*, 11953–11974. [CrossRef]
14. Cai, S.; Wu, C.; Yang, W.; Liang, W.; Yu, H.; Liu, L. Recent advance in surface modification for regulating cell adhesion and behaviors. *Nanotechnol. Rev.* **2020**, *9*, 971–989. [CrossRef]
15. Miller, D.J.; Paul, D.R.; Freeman, B.D.; Dreyer, D.R.; Bielawski, C.W. Surface modification of water purification membranes. *Angew. Chem. Int. Ed.* **2017**, *56*, 4662–4711. [CrossRef]
16. Chu, P.K.; Chen, J.Y.; Wang, L.P.; Huang, N. Plasma-surface modification of biomaterials. *Mater. Sci. Eng. R Rep.* **2002**, *36*, 143–206. [CrossRef]

17. Butt, M.A. Thin-film coating methods: A successful marriage of high-quality and cost-effectiveness-a brief exploration. *Coatings* **2022**, *12*, 1115. [CrossRef]
18. Mbam, S.O.; Gou, X.-F.; Nwigwe, U.S.; Nwonu, S.E.; Orelaja, O.A. Thin-film coating; historical evolution, conventional deposition technologies, stress-state micro/nano-level measurement/models and prospects projection: A critical review. *Mater. Res. Express* **2019**, *6*, 122001. [CrossRef]
19. Tang, C.Y.; Kwon, Y.N.; Leckie, J.O. Effect of membrane chemistry and coating layer on physiochemical properties of thin film composite polyamide Ro and Nf membranes. I. FTIR and XPS characterization of polyamide and coating layer chemistry. *Desalination* **2009**, *242*, 149–167. [CrossRef]
20. Sun, T.; Jiang, L.; Feng, L.; Gao, X. Bioinspired surfaces with special wettability. *Acc. Chem. Res.* **2005**, *38*, 644–652. [CrossRef] [PubMed]
21. Wang, S.; Li, X.; Wu, H.; Tian, Z.; Xin, Q.; He, G.; Peng, D.; Chen, S.; Jiang, Z.; Guiver, M.D.; et al. Advances in high permeability polymer-based membrane materials for CO_2 separations. *Energy Environ. Sci.* **2016**, *9*, 1863–1890. [CrossRef]
22. Zhu, T.; Li, J. Ultra-strength materials. *Prog. Mater. Sci.* **2010**, *55*, 710–757. [CrossRef]
23. Nazarov, V.G.; Doronin, F.A.; Evdokimov, A.G.; Dedov, A.V. Regulation of the Wettability of Nonwoven Cloth by Oxyfluorination to Improve its Impregnation by Latex. *Fibre Chem.* **2020**, *52*, 109–111. [CrossRef]
24. Li, X.; Chang, L.; Luo, S.; Yang, R.; Hou, Z.; Zou, J. Fe doping of carbon-coated manganese-rich cathode based on optimized preparation process to inhibit lattice distortion: Modification under optimal conditions. *Ceram. Int.* **2025**, *51*, 9039–9047. [CrossRef]
25. Gunka, V.; Bilushchak, H.; Prysiazhnyi, Y.; Demchuk, Y.; Hrynchuk, Y.; Sidun, I.; Shyshchak, O.; Bratychak, M. Production of bitumen modified with low-molecular organic compounds from petroleum residues. 4. Determining the optimal conditions for tar modification with formaldehyde and properties of the modified products. *Chem. Chem. Technol.* **2022**, *16*, 142–149. [CrossRef]
26. Liang, X.; Dong, J.; Wei, G.; Offiong, N.A.; Yang, C. Colloidal biliquid aphron demulsification using polyaluminum chloride and density modification of DNAPLS: Optimal conditions and common ion effect. *Environ. Sci. Process. Impacts* **2020**, *22*, 1908–1915. [CrossRef] [PubMed]
27. Cardoso, V.F.; Ribeiro, C.; Fernandes, M.M.; Correia, D.M.; Lanceros-Méndez, S. Fluorinated polymers as smart materials for advanced biomedical applications. *Polymers* **2018**, *10*, 161. [CrossRef] [PubMed]
28. Xiang, H.; Li, X.; Wu, B.; Sun, S.; Wu, P. Highly damping and self-healable ionic elastomer from dynamic phase separation of sticky fluorinated polymers. *Adv. Mater.* **2023**, *35*, 2209581. [CrossRef]
29. Kim, M.P.; Lee, Y.; Park, J.; Kim, J.; Ko, H.; Hur, Y.H.; Song, S.W.; Jung, Y.S.; Ahn, C.W. Molecular structure engineering of dielectric fluorinated polymers for enhanced performances of triboelectric nanogenerators. *Nano Energy* **2018**, *53*, 37–45. [CrossRef]
30. Giannetti, E. Thermal stability and bond dissociation energy of fluorinated polymers: A critical evaluation. *J. Fluor. Chem.* **2005**, *126*, 625–632. [CrossRef]
31. Ciardelli, F.; Aglietto, M.; Montagnini di Mirabello, L.; Passaglia, E.; Giancristoforo, S.; Castelvetro, V.; Ruggeri, G. New fluorinated acrylic polymers for improving weatherability of building stone materials. *Prog. Org. Coat.* **1997**, *32*, 43–50. [CrossRef]
32. Liu, Y.; Chen, Q.; Du, X.; Li, L.; Li, P. Surface modification of polyethylene terephthalate films by direct fluorination. *AIP Adv.* **2018**, *8*, 125333. [CrossRef]
33. Pilati, F.; Montecchi, M.; Fabbri, P.; Synytska, A.; Messori, M.; Toselli, M.; Grundke, K.; Pospiech, D. Design of surface properties of pet films: Effect of fluorinated block copolymers. *J. Colloid Interface Sci.* **2007**, *315*, 210–222. [CrossRef] [PubMed]
34. Cheng, T.S.; Lin, H.T.; Chuang, M.J. Surface fluorination of polyethylene terephthalate films with RF plasma. *Mater. Lett.* **2004**, *58*, 650–653. [CrossRef]
35. Kong, F.; Ma, Y.; Zhang, C.; Ren, C.; Shao, T.; Chang, C. Surface modifications of polystyrene and their stability: A comparison of DBD plasma deposition and direct fluorination. *Appl. Surf. Sci.* **2018**, *459*, 300–308. [CrossRef]
36. Kharitonov, A.P.; Moskvin, Y.u.L. Direct fluorination of polystyrene films. *J. Fluor. Chem.* **1998**, *91*, 87–93. [CrossRef]
37. Kharitonov, A.P. Direct fluorination of polymers-from fundamental research to industrial applications. *Prog. Org. Coat.* **2008**, *61*, 192–204. [CrossRef]
38. Kharitonov, A.P.; Taege, R.; Ferrier, G.; Teplyakov, V.V.; Syrtsova, D.A.; Koops, G.H. Direct fluorination—Useful tool to enhance commercial properties of polymer articles. *J. Fluor. Chem.* **2005**, *126*, 251–263. [CrossRef]
39. Doronin, F.; Rytikov, G.; Evdokimov, A.; Rudyak Yu Taranets, I.; Nazarov, V. The effect of electro-induced multi-gas modification on polymer substrates' surface structure for additive manufacturing. *Processes* **2023**, *11*, 774. [CrossRef]
40. Nazarov, V.G.; Stolyarov, V.P.; Doronin, F.A.; Evdokimov, A.G.; Rytikov, G.O.; Brevnov, P.N.; Zabolotnov, A.S.; Novokshonova, L.A.; Berlin, A.A. Comparison of the effects of some modification methods on the characteristics of ultrahigh-molecular-weight polyethylene and composites on its basis. *Polym. Sci. Ser. A* **2019**, *61*, 325–333. [CrossRef]
41. Sevast'yanov, V.I.; Nemets, E.A.; Stolyarov, V.P.; Baranov, V.A.; Bozhko, N.N.; Nazarov, V.G. Comparative study of the influence of polyethylene film surface modification on interaction with blood components. *Inorg. Mater. Appl. Res.* **2011**, *2*, 146–152. [CrossRef]
42. Doronin, F.; Rytikov, G.; Evdokimov, A.; Rudyak Yu Savel'ev, M.; Nazarov, V. Biostable fluorine-containing coatings on the surface of polymers. *Coatings* **2023**, *13*, 424. [CrossRef]

43. Doronin, F.A.; Rudakova, A.; Rytikov, G.O.; Nazarov, V.G. A novel determination of the melt flow index of composite filaments used in extrusion additive manufacturing. *Polym. Test.* **2024**, *133*, 108376. [CrossRef]
44. Song, X.; Liu, H.; Cheng, L.; Qu, Y. Surface modification of coconut-based activated carbon by liquid-phase oxidation and its effects on lead ion adsorption. *Desalination* **2010**, *255*, 78–83. [CrossRef]
45. Tsubota, T.; Tanii, S.; Ida, S.; Nagata, M.; Matsumoto, Y. Chemical modification of diamond surface with various carboxylic acids by radical reaction in liquid phase. *Diam. Relat. Mater.* **2004**, *13*, 1093–1097. [CrossRef]
46. Lebedev-Stepanov, P.V.; Molchanov, S.P.; Ivanov, A.A.; Mitrokhin, V.P.; Yurasik, G.A.; Alfimov, M.V.; Kadushnikov, R.M.; Rubin, N.I.; Vlasov, K.O.; Nazarov, V.G. Self-assembly of nanoparticles in the microvolume of colloidal solution: Physics, modeling, and experiment. *Nanotechnologies Russ.* **2013**, *8*, 137–162. [CrossRef]
47. Nazarov, V.G.; Stolyarov, V.P. Modified polymer substrates for the formation of submicron particle ensembles from colloidal solution. *Colloid J.* **2016**, *78*, 75–82. [CrossRef]
48. Kaneto, K.; Tsuruta, M.; Sakai, G.; Cho, W.Y.; Ando, Y. Electrical conductivities of multi-wall carbon nano tubes. *Synth. Met.* **1999**, *103*, 2543–2546. [CrossRef]
49. Chopra, N.; Majumder, M.; Hinds, B.J. Bifunctional carbon nano tubes by side wall protection. *Adv. Funct. Mater.* **2005**, *15*, 858–864. [CrossRef]
50. Joseph Berkmans, A.; Jagannatham, M.; Haridoss, P.; Priyanka, S. Synthesis of branched, nano channeled, ultrafine and nano carbon tubes from pet wastes using the arc discharge method. *Waste Manag.* **2014**, *34*, 2139–2145. [CrossRef]
51. Ma, L.; Luo, P.; He, Y.; Zhang, L.; Fan, Y.; Jiang, Z. Improving the stability of multi-walled carbon nano-tubes in extremely environments: Applications as nano-plugging additives in drilling fluids. *J. Nat. Gas Sci. Eng.* **2020**, *74*, 103082. [CrossRef]
52. Das, T.; Saikia, B.K.; Baruah, B.P. Formation of carbon nano-balls and carbon nano-tubes from northeast indian tertiary coal: Value added products from low grade coal. *Gondwana Res.* **2016**, *31*, 295–304. [CrossRef]
53. Clarke, D.R.; Oechsner, M.; Padture, N.P. Thermal-barrier coatings for more efficient gas-turbine engines. *MRS Bull.* **2012**, *37*, 891–898. [CrossRef]
54. Banerjee, I.; Pangule, R.C.; Kane, R.S. Antifouling coatings: Recent developments in the design of surfaces that prevent fouling by proteins, bacteria, and marine organisms. *Adv. Mater.* **2011**, *23*, 690–718. [CrossRef] [PubMed]
55. Musil, J. Hard and superhard nanocomposite coatings. *Surf. Coat. Technol.* **2000**, *125*, 322–330. [CrossRef]
56. Nazarov, V.G.; Stolyarov, V.P.; Gagarin, M.V. Simulation of chemical modification of polymer surface. *J. Fluor. Chem.* **2014**, *161*, 120–127. [CrossRef]
57. Nazarov, V.G.; Gagarin, M.V.; Stolyarov, V.P.; Evlampieva, L.A.; Baranov, V.A. Modeling of sliding friction processes in surface/spatial modified elastomer-metal couple. *Inorg. Mater. Appl. Res.* **2010**, *1*, 162–166. [CrossRef]
58. Kharitonov, A.P.; Moskvin, Y.L.; Kharitonova, L.N.; Kotenko, A.A.; Tulskii, M.N. Kinetics of gas-phase fluorination of homogeneous films and composite membranes based on polycarbonate siloxane and block-copolymer of polysulfone and polybutadiene. *Kinet. Catal.* **1994**, *35*, 792.
59. Kharitonov, A.P.; Moskvin, Y.L.; Kharitonova, L.N.; Tulskii, M.N.; Kotenko, A.A. An investigation into the direct fluorination kinetics of polymeric membranes. *Mendeleev Commun.* **1994**, *4*, 91. [CrossRef]
60. Nandiyanto, A.B.D.; Fiandini, M.; Ragadhita, R.; Sukmafitri, A.; Salam, H.; Triawan, F. Mechanical and biodegradation properties of cornstarch-based bioplastic material. *Mater. Phys. Mech.* **2020**, *44*, 380–391.
61. Doronin, F.A.; Saveliev, M.A.; Taranets, I.P.; Rytikov, G.O.; Nazarov, V.G. Direct Structuring of Polymers Used in Additive Manufacturing. *Russ. J. Gen. Chem.* **2024**, *94*, 1550–1557. [CrossRef]
62. Rytikov, G.O.; Pervoukhin, D.V.; Nazarov, V.G. A new approach to quantitative characterization of the material's surface morphological heterogeneity. *Lect. Notes Civ. Eng.* **2022**, *210*, 301–307.
63. Nandiyanto, A.B.D.; Oktiani, R.; Ragadhita, R. How to read and interpret FTIR spectroscope of organic material. *Indones. J. Sci. Technol.* **2019**, *4*, 97–118. [CrossRef]
64. Movasaghi, Z.; Rehman, I.U.; Rehman, S. Fourier transform infrared (FTIR) spectroscopy of biological tissues. *Appl. Spectrosc. Rev.* **2008**, *43*, 134–179. [CrossRef]
65. Madejova, J. FTIR techniques in clay mineral studies. *Vib. Spectrosc.* **2003**, *31*, 1–10. [CrossRef]
66. Bogner, A.; Jouneau, P.H.; Thollet, G.; Basset, D.; Gauthier, C. A history of scanning electron microscopy developments: Towards "wet-stem" imaging. *Micron* **2007**, *38*, 390–401. [CrossRef]
67. Brodowski, S.; Haumaier, L.; Zech, W.; Amelung, W.; Abetz, C. Morphological and chemical properties of black carbon in physical soil fractions as revealed by scanning electron microscopy and energy-dispersive x-ray spectroscopy. *Geoderma* **2005**, *128*, 116–129. [CrossRef]
68. Bootz, A.; Kreuter, J.; Vogel, V.; Schubert, D. Comparison of scanning electron microscopy, dynamic light scattering and analytical ultracentrifugation for the sizing of poly(butyl cyanoacrylate) nanoparticles. *Eur. J. Pharm. Biopharm.* **2004**, *57*, 369–375. [CrossRef]
69. Huckabay, H.A.; Armendariz, K.P.; Newhart, W.H.; Wildgen, S.M.; Dunn, R.C. Near-field scanning optical microscopy for high-resolution membrane studies. *Methods Mol. Biol.* **2013**, *950*, 373–394.

70. García, R.; Pérez, R. Dynamic atomic force microscopy methods. *Surf. Sci. Rep.* **2002**, *47*, 197–301. [CrossRef]
71. Carpick, R.W.; Salmeron, M. Scratching the surface: Fundamental investigations of tribology with atomic force microscopy. *Chem. Rev.* **1997**, *97*, 1163–1194. [CrossRef]
72. Drozdov, S.A.; Nazarov, V.G.; Nozdrachev, S.A.; Rudyak, Y.u.V.; Rytikov, G.O. The polymer composites' morphological structure simulation. *Nanosyst. Phys. Chem. Math.* **2017**, *8*, 137–145. [CrossRef]
73. Rytikov, G.O.; Doronin, F.A.; Evdokimov, A.G.; Nazarov, V.G.; Savel'ev, M.A. An approach to structural and functional modeling of the surface morphology of materials based on fluorinated polymers. *Russ. J. Gen. Chem.* **2021**, *91*, 2667–2672. [CrossRef]
74. Doronin, F.A.; Evdokimov, A.G.; Rudyak, Y.u.V.; Rytikov, G.O.; Taranets, I.P.; Nazarov, V.G. A new approach to function-structure modeling of the surface modified polymers. *Nanosyst. Phys. Chem. Math.* **2022**, *13*, 115–127. [CrossRef]
75. Doronin, F.A.; Rytikov, G.O.; Evdokimov, A.G.; Ruduak, Y.V.; Nazarov, V.G. The synergistic effect of bulk-surface modification onto the wear resistance of the ultrahigh molecular weight polyethylene. *Polym. Polym. Compos.* **2023**, *31*, 09673911221150132. [CrossRef]
76. Jorge, A.M.; Coutinho, J.A.; Pereira, J.F. Owens-Wendt method as a tool to evaluate polarity of polymer-polymer aqueous two-phase systems. *Colloids Surf. A Physicochem. Eng. Asp.* **2025**, *726*, 138080. [CrossRef]
77. Hong, G.; Cheng, H.; Meng, Y.; Lin, J.; Chen, Z.; Zhang, S.; Song, W. Mussel-Inspired Polydopamine as a Green, Efficient, and Stable Platform to Functionalize Bamboo Fiber with Amino-Terminated Alkyl for High Performance Poly(butylene succinate) Compo-sites. *Polymers* **2018**, *10*, 461. [CrossRef] [PubMed]
78. Waldner, C.; Hirn, U. Modeling liquid penetration into porous materials based on substrate and liquid surface energies. *J. Colloid Interface Sci.* **2023**, *640*, 445–455. [CrossRef]
79. Fowkes, F.M. Additivity of Intermolecular Forces at Interfaces. I. Determination of the Contribution to Surface and Interfacial Tensions of Dispersion Forces in Various Liquids1. *J. Phys. Chem.* **1963**, *67*, 2538–2541. [CrossRef]
80. Good, R.J. *Contact Angle, Wettability and Adhesion*; Mittal, K.L., Ed.; VSP: Utrecht, The Netherlands, 1993.
81. Parale, V. Effect of surface composition and roughness on the apparent surface free energy of silica aerogel materials. *Appl. Phys. Lett.* **2011**, *99*, 104104. [CrossRef]
82. Selvakumar, N.; Barshilia, H.C.; Rajam, K.S. Effect of substrate roughness on the apparent surface free energy of sputter deposited superhydrophobic polytetrafluoroethylene coatings: A com-parison of experimental data with different theoretical models. *J. Appl. Phys.* **2010**, *108*, 013505. [CrossRef]
83. Laput, O.; Vasenina, I.; Salvadori, M.C.; Savkin, K.; Zuza, D.; Kurzina, I. Low-temperature plasma treatment of polylactic acid and PLA/HA composite material. *J. Mater. Sci.* **2019**, *54*, 11726–11738. [CrossRef]
84. Xie, Y.; Zhu, J.; Fu, L.; Yang, W.; Li, D.; Zhou, L. TPU with outstanding wettability and hydrophilic stability is obtained by plasma-induced graft polymerization. *Appl. Surf. Sci.* **2024**, *654*, 159509. [CrossRef]
85. Chen, T.; Zhang, J. Surface hydrophilic modification of acrylonitrile-butadiene-styrene terpolymer by poly(ethylene glycol-co-1,4-cyclohexanedimethanol terephthalate): Preparation, characterization, and properties studies. *Appl. Surf. Sci.* **2016**, *388 Pt A*, 133–140. [CrossRef]
86. Nazarov, V.G.; Doronin, F.A.; Evdokimov, A.G.; Rytikov, G.O.; Stolyarov, V.P. Oxyfluorination-Controlled Variations in the Wettability of Polymer Film Surfaces. *Colloid J.* **2019**, *81*, 146–157. [CrossRef]
87. Taranets, I.P.; Rytikov, G.O.; Doronin, F.A.; Saveliev, M.A.; Nazarov, V.G. Structural-Functional Mathematical Modeling of Additive Manufacturing Polymers. *Russ. J. Gen. Chem.* **2024**, *94*, 1558–1563. [CrossRef]
88. Datta, J.; Kasprzyk, P. Thermoplastic Polyurethanes Derived From Petrochemical or Renewable Resources: A Comprehensive Review. *Polym. Eng. Sci.* **2017**, *58*, E14–E35. [CrossRef]
89. Suthapakti, K.; Molloy, R.; Leejarkpai, T. Disintegration Testing of Biodegradable Poly(L-lactide)/Thermoplastic Polyurethane Melt Blended Films. *Chiang Mai J. Sci.* **2018**, *45*, 2079–2091.
90. Beeker, L.Y.; Pringle, A.M.; Pearce, J.M. Open-source parametric 3-D printed slot die system for thin film semiconductor processing. *Addit. Manuf.* **2018**, *20*, 90–100. [CrossRef]
91. Jin, X.; Wang, F.; Wang, Z.; Yang, Y.; Chu, Z.; Guo, N.; Lv, X. Research on Micro-Mechanics Modelling of TPU-Modified Asphalt Mastic. *Coatings* **2022**, *12*, 1029. [CrossRef]

Disclaimer/Publisher's Note: The statements, opinions and data contained in all publications are solely those of the individual author(s) and contributor(s) and not of MDPI and/or the editor(s). MDPI and/or the editor(s) disclaim responsibility for any injury to people or property resulting from any ideas, methods, instructions or products referred to in the content.